

Supermassive Black Hole Seed Formation at High Redshifts: Long-Term Evolution of the Direct Collapse

Isaac Shlosman^{1,2*}, Jun-Hwan Choi^{3†}, Mitchell C. Begelman^{4,5}, Kentaro Nagamine^{2,6}

¹ *Department of Physics & Astronomy, University of Kentucky, Lexington, KY 40506-0055, USA*

² *Theoretical Astrophysics, Department of Earth & Space Science, Graduate School of Science, Osaka University, Osaka 560-0043, Japan*

³ *Department of Astronomy, University of Texas, Austin, TX 78712-1205, USA*

⁴ *JILA, University of Colorado and National Institute of Standards and Technology, 440 UCB, Boulder, CO 80309-0440, USA*

⁵ *Department of Astrophysical and Planetary Sciences, 391 UCB, Boulder, CO 80309-0391, USA*

⁶ *Department of Physics & Astronomy, University of Nevada, Las Vegas, NV 89154-4002, USA*

Accepted 2015 November 16; Received 2015 November 10; in original form 2015 August 18

ABSTRACT

We use cosmological adaptive mesh refinement (AMR) code Enzo zoom-in simulations to study the long term evolution of the collapsing gas within dark matter halos at z . This direct collapse process is a leading candidate for rapid formation of supermassive black hole (SMBH) seeds. To circumvent the Courant condition at small radii, we apply the sink particle method, focusing on evolution on scales $\sim 0.01 - 10$ pc. The collapse proceeds in two stages, with the secondary runaway happening within the central 10 pc. The sink particles form when the collapsing gas requires additional refinement of the grid size at the highest refinement level. Their growth is negligible with the sole exception of the central seed which grows dramatically to $M_{\text{seed}} \sim 2 \times 10^6 M_{\odot}$ in ~ 2 Myr, confirming the feasibility of this path to the SMBH. The variability of angular momentum in the accreted gas results in the formation of two misaligned disks. Both disks lie within the Roche limit of the central seed. While the inner disk is geometrically thin and weakly asymmetric, the outer disk flares due to turbulent motions as a result of the massive inflow along a pair of penetrating filaments. The filamentary inflow determines the dominant Fourier modes in this disk — these modes have a non-self-gravitational origin. We do not confirm that $m = 1$ is a dominant mode that drives the inflow in the presence of a central massive object. The overall configuration appears to be generic, and is expected to form when the central seed becomes sufficiently massive.

Key words: methods: numerical — galaxies: formation — galaxies: high-redshift — cosmology: theory — cosmology: dark ages, reionization, first stars

1 INTRODUCTION

Supermassive black holes (SMBHs) formed early in the history of the universe. Luminous quasars have been observed up to redshifts $z \sim 7.1$ (e.g., Fan et al. 2003; Mortlock et al. 2011; Wu et al. 2015), and have been estimated to host SMBHs in excess of $10^9 M_{\odot}$, just 700 Myr after the Big Bang. Unless the SMBHs are primordial, they must have formed by the accumulation of matter during the epoch of galaxy formation — either as remnants of the Population III stars (e.g., Haiman & Loeb 2001; Abel et al. 2002; Bromm & Larson 2004; Volonteri & Rees

2006; Li et al. 2007; Pelupessy et al. 2007), or the end products of gas collapse into dark matter (DM) halos with virial temperatures $\gtrsim 10^4$ K (e.g., Haehnelt & Rees 1993; Oh & Haiman 2002; Bromm & Loeb 2003; Volonteri & Rees 2006; Begelman et al. 2006; Begelman & Shlosman 2009; Milosavljević et al. 2009; Mayer et al. 2010; Schleicher et al. 2010; Hosokawa et al. 2011; Johnson et al. 2011; Choi et al. 2013, 2015; Latif et al. 2013; Prieto et al. 2013). Accounting for radiative feedback during formation of Pop III stars lowers their main sequence masses to be more in line with those of normal stars. The black hole remnants are downsized as well, to $\sim 10 M_{\odot}$, making it exceedingly difficult to explain the growth of early SMBHs from Pop III seeds. Furthermore, recent results from Planck have pushed the beginning of the Pop III epoch forward from ~ 400 Myr to ~ 560 Myr after

* E-mail: shlosman@pa.uky.edu

† E-mail: jhchoi@astro.as.utexas.edu

the Big Bang (e.g., Planck Collaboration et al. 2015). Taken together, these arguments favor substantially more massive SMBH seeds, $\sim 10^5 - 10^7 M_\odot$, as the direct collapse models suggest.

Important details of direct collapse remain unclear, e.g., how does the process evolve when the flow becomes optically thick to internally produced radiation? How is angular momentum redistributed during the optically-thick regime? Does the collapse lead to a hydrostatically supported supermassive star (SMS) — a precursor to SMBH seed formation (e.g., Begelman 2010) — or does the flow remain disk-like and by-pass the SMS and the associated thermonuclear stage (Choi et al. 2013)?

On the other hand, we now understand some of the details of the collapse in the optically-thin regime. The fragmentation of the flow is damped by the dominant gravitational potential of the host DM halo and by virial supersonic turbulence — both of which substantially increase the Jeans mass of the gas. Furthermore, the DM acts as a sink of the angular momentum from the collapsing gas, both in isolated collapse models and in the cosmological context (e.g., Wise et al. 2008; Begelman & Shlosman 2009; Choi et al. 2013, 2015).

Studies of the direct collapse to form the SMBH seeds involve computationally-intensive efforts to follow the hydrodynamics and the thermal state of the collapsing gas. Processes like fragmentation, star formation, redistribution of angular momentum in the collapsing flow, development of a supersonic turbulence, etc., can be addressed only numerically.

Typically, the collapse region extends over many orders of magnitude in radius, from a few kpc down to $\sim 1 - 100$ AU. Even sophisticated methods face difficulties in dealing with such an extended dynamic range. As the collapse progresses, the simulation timesteps become increasingly short, making it prohibitively expensive to follow the evolution. Moreover, the buildup of the optical depth in the flow can fully or partially trap the radiation produced in situ, affecting the dynamics and thermodynamics of the collapsing gas.

Two options have been proposed to overcome these obstacles. The first involves (consecutive) zoom-in simulations typically associated with calculations of cosmological structure formation and galaxy evolution (e.g., Becerra et al. 2015). This method allows one to increase the mass and spatial resolution of the model, especially on the smallest scales, to introduce various physical processes, on different scales, and to avoid artefacts associated with a small number of particles or grid cells at small radii. Becerra et al. (2015) have assumed that the radiative cooling becomes inefficient at some presumed radius. Such an exponential cutoff in the cooling rate naturally leads to a radiation pressure-dominated entity — an SMS. By itself this does not resolve the issue of radiation trapping in the flow — in a 3-D rotation-dominated inflow the radiation, in principle, can escape. It does not allow one to study the optically thin-to-thick transition in the flow and the nature of the flow inside the optically-thick region. Merely increasing the mass and spatial resolutions will not resolve the problem and will not allow one to prolong the simulation without also introducing additional physical processes such as radiative transfer and associated dynamical effects. At present time, sufficiently

powerful radiation hydrodynamics codes are not generally available.

The second option involves the sink particle method, successfully applied to star formation and other problems to focus on a specific range in radius, preventing the smaller scales from forcing an increasingly small timestep, and thus enabling one to follow the long-term evolution of the collapsing flow (e.g., Bate et al. 1995; Krumholz et al. 2004; Federrath et al. 2010; Wang et al. 2010; Teysier et al. 2011; Gong & Ostriker 2013). In this method, gas on small spatial scales is replaced by the sink particles, which can grow in mass as the surrounding gas evolves.

In this paper, we apply the sink particle method to the direct collapse problem in a cosmological framework. We focus on the long-term evolution of the flow and on associated processes on scales of $\sim 0.01 - 10$ pc, deep inside the DM halo gravitational potential. The choice of this scale is based on purely numerical reasons, in order to circumvent the exceedingly small timestep. It also allows us to avoid additional physical processes on the small scale, such as radiative transfer, without any loss of generality.

Starting with our cosmological simulations of direct collapse (Choi et al. 2015), we create sink particles in the flow (as described in Section 2), and analyze motions and growth of these particles and their effect on the collapse itself. Choi et al. has followed the collapse down to $\sim 10^{-4}$ pc scales, where one anticipates trapping of the continuum photons produced in the flow and the formation of a photosphere. Of course, the Lyman α photons are trapped or at least partially trapped already at larger radii. Here we ignore scales smaller than ~ 0.01 pc, which allows us to continue following the collapse on scales > 0.01 pc, over timescales much longer than those simulated by Choi et al.

This paper is structured as follows. Section 2 provides the details of our numerical technique and explains the sink particle method implemented here. We present our results in Section 3 and discuss them in the last section.

2 NUMERICAL TECHNIQUES

2.1 Simulations

We use the Eulerian adaptive mesh refinement (AMR) code Enzo-2.3, which has been tested extensively and is publicly available (Bryan & Norman 1997; Norman & Bryan 1999; Bryan et al. 2014). Enzo uses a particle-mesh N -body method to calculate the gravitational dynamics, including collisionless DM particles, and a second-order piecewise parabolic method (PPM, Bryan et al. 1995) to solve hydrodynamics. The structured AMR used in Enzo places no fundamental restrictions on the number of rectangular grids used to cover some region of space at a given level of refinement, or on the number of levels of refinement (Berger & Colella 1989). A region of the simulation grid is refined by a factor of 2 in lengthscale, if either the gas or DM density become greater than $\rho_{0,\text{gas,dm}} N^l$, where $\rho_{0,\text{gas,dm}}$ is the cosmic mean density for the gas or DM respectively, $N = 2$ is the refinement factor, and l is the maximal AMR refinement level.

The Jeans length has been resolved by at least 16 cells in the simulations. Hence, the Truelove et al. (1997) requirement for resolution of the Jeans length (see Section 2.3),

i.e., at least four cells, has been superseded substantially (e.g., Sur et al. 2010; Federrath et al. 2011; Turk et al. 2012; Latif et al. 2013).

Enzo follows the non-equilibrium evolution of six species: H, H⁺, He, He⁺, He⁺⁺, and e⁻ (Abel et al. 1997; Anninos et al. 1997) in a gas with a primordial composition. It calculates radiative heating and cooling following atomic line excitation, recombination, collisional excitation and free-free transitions. Radiative losses from atomic cooling are computed in the optically-thin limit.

Several radiation processes which prevent H₂ formation in the collapsing flow have been proposed (e.g., Omukai 2001; Spaans & Silk 2006; Schleicher et al. 2010; Latif et al. 2011; Choi et al. 2013; Inayoshi et al. 2014; Sugimura et al. 2014). In this work we assume that H₂ does not form and exclude the chemistry and cooling related to H₂, which simplifies the chemical evolution.

2.2 Zoom-in initial conditions

We follow the long-term dynamical evolution of the collapsing gas within a DM halo in a fully cosmological environment and subject to atomic cooling. To satisfy the resolution requirement, we use the MUSIC code (Hahn & Abel 2011) to generate the cosmological zoom-in initial conditions (ICs). MUSIC uses a real-space convolution approach in conjunction with an adaptive multi-grid Poisson solver to generate highly accurate nested density, particle displacement, and velocity fields suitable for multi-scale zoom-in simulations of structure formation in the universe.

Generating a set of “zoom-in” ICs is a two-step process. First, we generate $1h^{-1}$ Mpc comoving 128^3 DM-only ICs for the pathfinder simulation and run it without AMR until $z = 10$. Using the HOP group finder (Eisenstein & Hut 1998), we select an appropriate DM halo, whose mass is $\sim 10^8 h^{-1} M_{\odot}$ at $z = 10$. Secondly, we generate $1h^{-1}$ Mpc ICs with 512^3 resolution in DM and gas in the zoom-in region. Since we use the same random seeds of these ICs as the ICs at the first step, the phases of both ICs are identical. The zoom-in region is centered on the selected halo position and is set to be large enough to cover the initial positions of all selected halo particles.

The ICs are generated using WMAP5 cosmology: $\Omega_{\Lambda} = 0.721$, $\Omega_{\text{m}} = 0.279$, $\Omega_{\text{b}} = 0.0445$, $h = 0.701$, $\sigma = 0.807$, and $n_{\text{e}} = 0.961$. In the following we use R for spherical coordinates and r for cylindrical ones.

2.3 Sink particle algorithm

Sink particles are used in order to weaken the Courant conditions restrictions on the timestep. The restriction can result from the increase in the local density of the gas and demand for additional refinement (i.e. spatial resolution). Under these circumstances, it is nearly impossible to study the large-scale, long-term evolution of the direct collapse within DM halos. To circumvent these numerical obstacles, we adopt the sink particle method to model the gravitational collapse. This is especially relevant for the present work, which aims at long-term evolution of the direct collapse. Before the gas density exceeds that of the DM density, at $t \sim 350$ Myr, sink particles are not used. However, after

the gas decouples, its central density increases rapidly. Below we describe the specifics of this method.

Various works have invoked sink particles in order to advance their goals (e.g., Bate et al. 1995; Krumholz et al. 2004; Federrath et al. 2010; Wang et al. 2010; Teyssier et al. 2011; Gong & Ostriker 2013). We implement the sink particle method largely based on Wang et al. (2010), who studied massive star formation using Enzo AMR simulations. We require a sink particle to form when the cell violates the refinement criterion at the highest refinement level in the collapsing part of the flow.

When this happens, a sink particle is inserted at the center of the cell. The initial sink particle mass is computed based on the mass exceeding the maximum allowed density at a maximum refinement level. In other words, each cell density has a maximal value that does not violate the refinement criterion. The initial sink particle velocity is calculated based on linear momentum conservation.

After a sink particle is formed, it accretes the gas from its host cell according to following prescription:

$$\dot{M}_{\text{sp}} = 4\pi\rho_{\text{out}}r_{\text{B}}^2\sqrt{1.2544c_{\text{cell}}^2 + v_{\text{rel}}^2}, \quad (1)$$

where \dot{M}_{sp} is the mass growth rate of a sink particle, $\rho_{\text{out}} = \rho_{\text{cell}} \min[1.0, (l_{\text{cell}}/r_{\text{B}})^{1.5}]$, l_{cell} is the cell size, $r_{\text{B}} = GM_{\text{sp}}/(c_{\text{cell}}^2 + v_{\text{rel}}^2)$ is the Bondi accretion radius, c_{cell} is the sound speed in the cell, and v_{rel} is the relative velocity between the host cell and the sink particle.

Merging between sink particles is a necessary process in order to accurately estimate their mass growth rate and to reduce the computational cost. In principle, the sink particles represent overdense gas clumps in our simulations whose internal evolution we ignore. We require two sink particles to merge when their separation becomes smaller than $5l_{\text{cell}}$, and assume that the less massive sink particle merges with the more massive one. The merging process is quite insensitive to the definition of the critical separation between particles (e.g., Wang et al. 2010). We have confirmed this by comparing various maximal refinement levels.

In this paper, we use three different maximum refinement levels that affect the overall simulation resolution and the scale of the sink particle formation. The maximal AMR refinement level l (see Section 2.1) is 10 in run L10, $l = 12$ in run L12, and $l = 15$ in run L15. The maximal spatial resolution corresponds to ~ 0.1 pc for run L12 and to ~ 0.01 pc for run L15.

All three simulations have been restarted from the cosmological run described in Choi et al. (2015), at $t \sim 355$ Myr, when the refinement level in the gas is $l = 8$, and when the gas-to-DM density ratio in the central ~ 10 pc is about unity. They are identical simulations except for the maximal AMR level. While our analysis here is based on run L12, we use runs L10 and L15 to test convergence of the observed evolution.

3 RESULTS

The DM halo under investigation has been selected from a computational box containing several such objects at $z = 10$. This halo has been re-simulated at high resolution down to $z \sim 12$, or $t \sim 355$ Myr from the Big Bang, when it

reached the virial mass and radius of $M_h \sim 2 \times 10^7 h^{-1} M_\odot$ and $R_{\text{vir}} \sim 10 h^{-1} \text{kpc}$ in comoving coordinates, with a cosmological spin parameter $\lambda \sim 0.03$. At this time, the DM density profile can be approximated by an NFW profile (e.g., Navarro et al. 1997), with a characteristic scale radius of $R_s \sim 30 \text{pc}$, in physical coordinates, and with a concentration parameter $c \equiv R_{\text{vir}}/R_s \sim 25$. At about $t \sim 355 \text{Myr}$, the gas-to-DM density ratio exceeds unity interior to $\sim R_s$. The gas density quickly establishes a density profile slightly steeper than $\sim R^{-2}$, down to the limiting radius of $R \sim 10^{-4} \text{pc}$, imposing a tight Courant condition on the timestep.

As shown by Choi et al. (2013, 2015), direct collapse, in both the isolated case and in a cosmological framework, can be divided into two parts: the first stage ends when the central gas density reaches that of the DM, and the second stage begins when the central gas density exceeds that of the DM, and the gas effectively decouples from the DM. During this latter stage, an r^{-2} density profile is established all the way down to $\sim 10^{-4} \text{pc}$ — the region where the optical depth to continuum radiation produced by the accretion flow becomes larger than unity, the so-called thin-to-thick transition. As such a large dynamic range imposes a very strict condition on the timestep, and because we focus on the optically-thin part of the flow, we introduce sink particles based on the criteria discussed in Section 2.3. By doing this, we remove the smallest spatial scales, $r < 0.1 \text{pc}$ (for run L12) and $< 0.01 \text{pc}$ (for run L15), from consideration. Hence, these are the limiting resolutions of the models. On the other hand, we gain the ability to follow the collapse well beyond the time achieved in Choi et al. (2015).

3.1 Rapid growth of the central sink particle

The masses of sink particles introduced in the run L12 correspond to the gas mass of the smallest grid cells. Runs L10 and L15, in this respect, are very similar, but their resolutions are $\sim 1 \text{pc}$ and $\sim 0.01 \text{pc}$ respectively. So, the newly born particles provide only a negligible effect on the flow when they are introduced. They can grow by accretion and merging and, at least in principle, their influence grows. We find that sink particles appear always within the central $\sim 1 - 2 \text{pc}$, measured from the densest gas cell. Their number never substantially exceeds ~ 10 in the collapsing flow. They grow, but their individual masses stay below $\sim 10^3 M_\odot$. The sole exception is the sink particle that lies at the center. This particle grows fast, and in less than $\sim 2 \text{Myrs}$ surpasses $M_{\text{seed}} \sim 2 \times 10^6 M_\odot$, as shown in Figure 1. (We term this sink particle as a ‘seed’ and conjecture that its evolution is closely related to the future formation of the SMBH seed.) After this time, its growth rate saturates substantially. We separate these phases into dynamic and secular growth stages of the central seed.

For comparison, we also show the evolution of the central sink particle in runs L10 and L15. In run L10, the central sink particle starts to grow slightly earlier, but very quickly its growth curve merges with that of L12, even before the end of the dynamic stage. During the secular stage, the L10 growth rate initially exceeds that for L12. Asymptotically, the L10 and L12 growth rates are nearly identical, but the final seed masses differ by about 20%.

Run L15 displays a nearly identical growth for the cen-

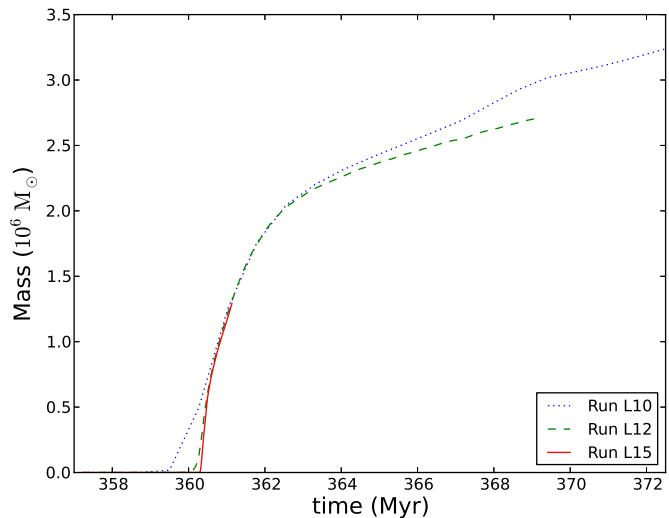


Figure 1. Evolution of the central sink particle mass, M_{seed} , forming at the position of the density peak for three different AMR runs, L10, L12 and L15. While L10 exhibits a somewhat slower or faster growth of the central seed at various times, L12 and L15 show virtually no difference. Note, that the initial growth of the seed mass is very rapid, so that it reaches $M_{\text{seed}} \sim 2 \times 10^6 M_\odot$ in $\lesssim 2 \text{Myr}$.

tral particle, except for very early times — growth is triggered slightly later but the rate is higher. We therefore, conclude that the resolution of run L12 is sufficient for our purpose, because the growth rates in L12 and L15 appear identical.

So, irrespective of the resolution we choose for the sink particles, the central seed grows in a very short time to exceed $10^6 M_\odot$. How is this mass converted into the SMBH seed is a subject for future research.

3.2 The central massive seed and disk formation

To understand the specifics of the growth of the central seed, we plot the evolution of the gas masses within the central 2 pc and 20 pc, and compare them with the mass of the central seed, the total mass of other (off-center) sink particles, and the DM within these spherical volumes. Note that the sink particles grow only by accreting gas and incorporating other sink particles, but not through accretion of DM. The total baryonic mass, i.e., the gas and the sink particles, is, therefore, conserved.

In Figure 2a, we observe that the total mass of the off-center sink particles in the region remains very small. The gas accumulation inside the innermost 2 pc starts around 358 Myr and peaks at $\sim 360 \text{Myr}$, prior to and concurrently with the formation and rapid growth of the central seed. After the rapid growth stage, the gas mass inside this region is remarkably constant at $\sim 10^4 M_\odot$, showing that *net* inflow into this region is negligible. Below, we discuss the detailed mass balance in the region. Note, that the gas at the peak inflow rate into this region drags in the DM, which dominates the gas mass during the secular evolution of the

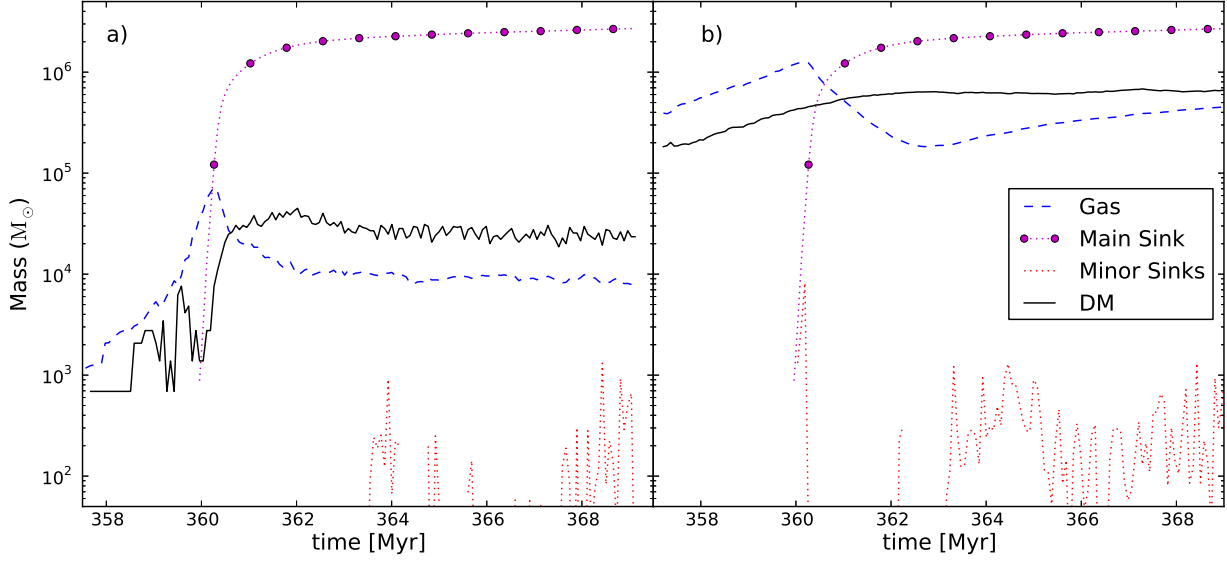


Figure 2. Evolution of masses within spherical volumes with a radius of 2 pc (left frame) and 20 pc (right frame). Shown are the gas mass (blue dashed line), DM mass (black solid line), central seed (dotted line with large dots), and the total of all minor sink particles (dotted green line).

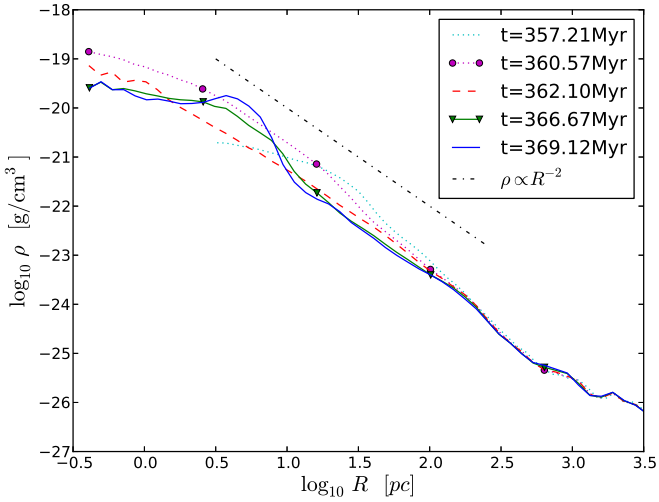


Figure 3. Evolution of the gas density profile for run L12. The density profiles, $\rho \sim r^{-\alpha}$, exhibit flattening in the central region, from $\alpha \sim 2$ to $\alpha \sim 0.5$, where the gas assembles into a disk structure around the central massive seed.

central sink. This provides additional stability against the gas fragmentation in the region.

The mass evolution within the central 20 pc paints a similar picture, with an important difference (Fig. 2b). The gas mass grows monotonically until the formation of the central seed, then drops by an order of magnitude during the 2 Myr rapid growth of the central seed. This explains the source of the mass in this seed. After this time, the gas mass continues to accumulate at nearly the original rate. The DM here experiences the same adiabatic contraction

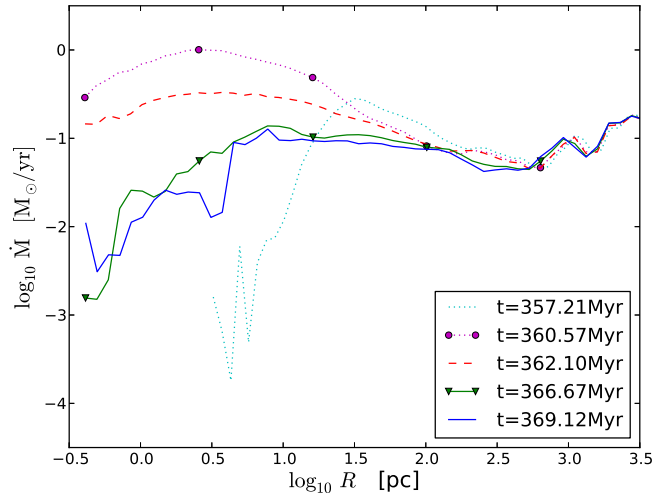


Figure 4. Evolution of the mass accretion rate profile for the L12 run. Note the sharp decrease in \dot{M} from the peak of $\sim 0.3 - 1 M_{\odot} \text{ yr}^{-1}$ by about two orders of magnitude at smaller radii, as a result of the rotational support achieved near the massive sink particle.

as in Figure 2a, and dominates the gas. It is clear, however, that the gas will shortly reverse this situation — as shown by Figure 2b, about 10 Myrs after the formation of the central seed, the gas mass in the region will surpass that of the DM, yet it will remain well below the mass of the central seed. We discuss reasons for the gas evolution in the vicinity of the central seed and its global consequences below and in Section 4.

The differences between gas evolution inside the central

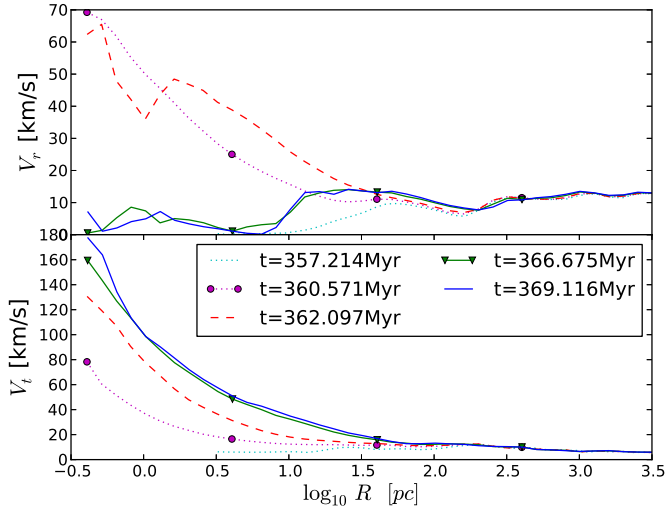


Figure 5. Evolution of the radial (top) and tangential (bottom) velocity profiles, v_r and v_t , in the gas for run L12. Note the sharp decrease in the central v_r and increase in the v_t there — a clear sign of disk formation.

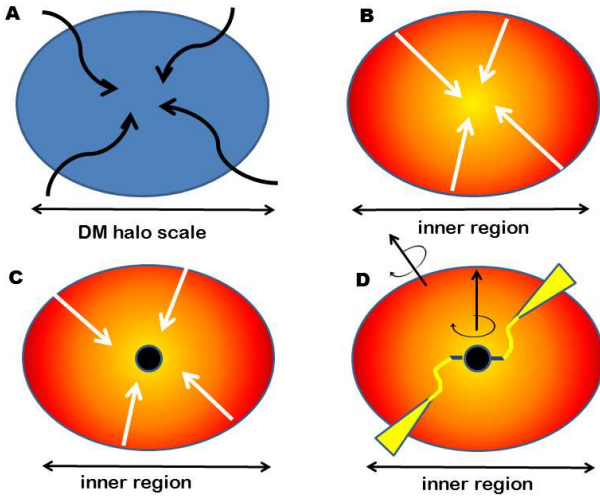


Figure 6. Schematic picture of various stages in the direct collapse with the rapidly growing central seed. *Stage A:* Filamentary inflow into the DM halo on scale of ~ 1 kpc; *Stage B:* Gas density exceeds the DM density and the secondary collapse is triggered. In the case of current simulation setup, the ‘inner region’ indicates roughly 20 pc region from the sink; *Stage C:* Central sink forms and rapidly grows to $\sim 10^6 M_\odot$; *Stage D:* High angular momentum gas accumulates in a system of misaligned disks (shown here edge-on), forming due to the fluctuating angular momentum of the collapsing gas. The small inner disk is shown horizontal, and the outer disk is inclined. The disks are connected by a symmetric warp. See also Figure 8 and explanations in the text.

region and on larger scales is related to the gas kinematics. This is seen in Figure 3, where the slope of the gas density within the central ~ 10 pc, $\rho \sim r^{-\alpha}$, changes from $\alpha \sim 2$ to ~ 0.5 — the gas density profile has flattened. Because we assume that the gas is optically-thin, the temperature profile remains the same as shown in Choi et al. (2015).

Another by-product of the change in the prevailing kinematics, is the evolution of the gas accretion rate profile. The peak accretion rate of $\sim 1 M_\odot \text{ yr}^{-1}$ inside ~ 10 pc is reached between $t \sim 360 - 362$ Myr (Fig. 4). This is reflected in the very fast growth of the central seed during these 2 Myr. Immediately after this, the radial profile of the mass accretion rate, $\dot{M}(r)$, drops dramatically from its peak by about two orders of magnitude or more with decreasing radius. That is, at $r \sim 10$ pc, the mass inflow rate stays approximately the same, $\sim 0.3 M_\odot \text{ yr}^{-1}$, but it declines sharply with radius to $\sim 3 \times 10^{-3} M_\odot \text{ yr}^{-1}$ at ~ 0.3 pc. Note, that substantial amount of gas, $\sim 6 \times 10^6 M_\odot$, resides in the DM halo outside 20 pc at the time of disk formation, and that the accretion rate onto the halo remains high as well.

This behavior in the gas density profile and its accretion rate within the central 20 pc means that the gas accumulates there at rapid pace. At around $t \sim 360$ Myr, this is related to the formation and a rapid growth of the central seed. However, after $t \sim 362$ Myr, this is the direct consequence of the accumulation of angular momentum and formation of a gaseous disk in this region.

Evolution of the mass accretion rate is clearly reflected in the abrupt collapse of the gas and formation of the central seed, and can be followed in the top frame of Figure 5. The radial velocity at $t \sim 360.6$ Myr increases to $\gtrsim 70 \text{ km s}^{-1}$. This is well above the virial velocity of the DM halo, by almost an order of magnitude, and can only result from the gravitational decoupling of the gas from the background DM potential. Rotational velocity around 0.3 pc from the central seed has reached $v_t \sim 160 \text{ km s}^{-1}$ by $t \sim 363.6$ Myr — exceeding the DM virial velocity by a factor of ~ 16 (Fig. 5, bottom frame). Hence the depth of the potential well due to the massive seed has substantially surpassed that in the DM. Basically, this corresponds to the following sequence of events: onset of gravitational collapse in the gas on scales $\lesssim 20$ pc, gravitational decoupling of the gas from the DM, formation of the massive seed, and continuing accretion onto this seed. At the same time, the increased rotational support for the gas can be clearly observed in a decreased radial inflow velocity to $v_r < 10 \text{ km s}^{-1}$, and a corresponding sharp increase in the tangential velocity, v_t , which develops a Keplerian profile inside the inner $r \sim 50$ pc, as seen in Figure 5.

The central seed has reached $M_{\text{seed}} \sim 10^4 M_\odot$ at $t \sim 360.1$ Myr. Strong compression of the collapsing gas, shocks, and radial filaments can be observed at this time. The disk first becomes visible at ~ 361.5 Myr, when $M_{\text{seed}} \sim 1.6 \times 10^6 M_\odot$, and can be seen in two out of three projection planes, xz (face-on) and xy (edge-on), initially on scales of the inner 2 – 3 pc. It grows rapidly in size, as a strong gaseous bar with two associated *open spirals*¹ become dominant around ~ 362.1 Myr. By ~ 362.7 Myr, the disk radius has reached ~ 5 pc. Around ~ 363.7 Myr, one starts to distinguish between an inner, geometrically thin disk, 2-3 pc in

¹ Such spirals signal efficient angular momentum loss by the gas.

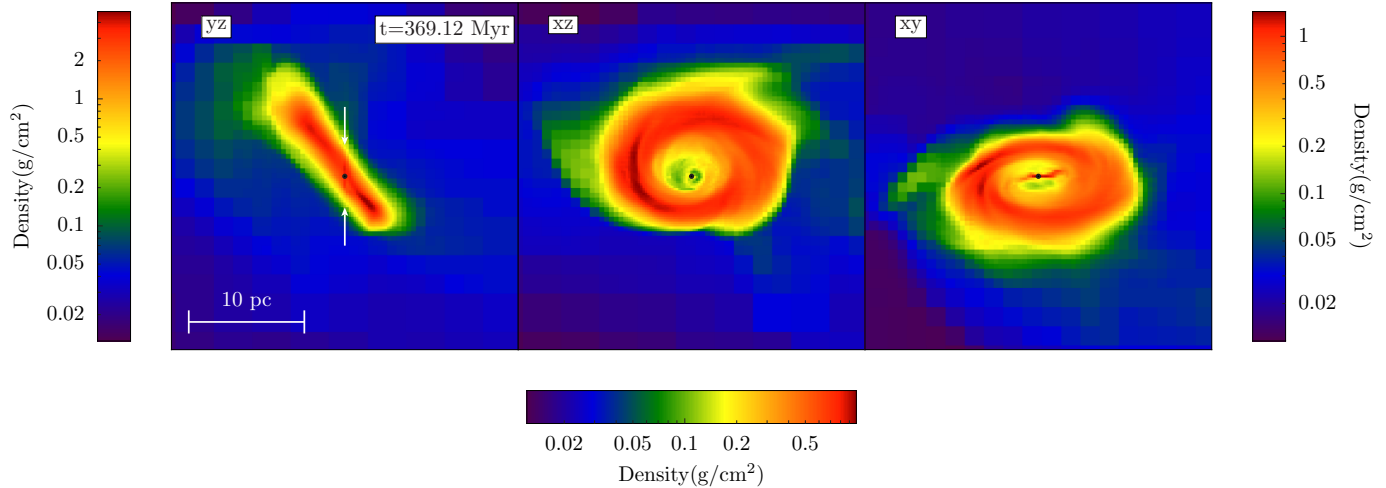


Figure 7. Gas column density normal to main planes at the end of the simulation, $t \sim 369$ Myr, for run L12. The left frame shows the inner edge-on disk (position delineated by the white arrows) embedded in the outer disk which is inclined by about 45° in the yz plane. The middle frame shows the same figure with the inner disk being face-on in the xz plane. The right frame shows another projection of the inner edge-on disk and the inclined (toward the observer) outer disk in the xy plane. The inner warp connection between the disks can be clearly seen in this projection. The position of the central seed is shown by a black point. The filaments which feed the outer disk are clearly visible.

radius, and an outer, much thicker disk, which is misaligned by about 45° with inner one. The overall radius of this configuration is about 10–12 pc. Formation of the outer inclined disk is the result of gas influx with a different direction of angular momentum into the region.

The stages of direct collapse are depicted schematically in Figure 6. Stage A of the collapse corresponds to the initial inflow into the DM halo. Stage B corresponds to the gas density exceeding that of the DM and dynamically decoupling from the background DM potential. Stage C culminates with the formation of the central seed and its runaway growth, and the last stage is associated with the formation of the misaligned disk system due to the fluctuating angular momentum of the accreting gas.

This configuration, of inner and outer disks being strongly misaligned, appears stable for the next ~ 6 Myr — a time period which corresponds to about 20–25 rotational periods at ~ 15 pc. By the end of the simulation, $t \sim 369.12$ Myr, the inner disk has a radius of 3–4 pc and the outer disk about 10–12 pc (Fig. 7). The thickness of the inner disk is $\lesssim 1$ pc, and that of the outer disk varies from $\lesssim 1$ pc to ~ 3 pc — this disk flares as seen in Figure 8 (bottom frames). The inner disk is connected to the outer one with a clearly visible symmetric, integral-shaped warp.

We do not observe any fragmentation in the inner and outer disks. Why is the fragmentation suppressed in the disks, where a high-density, low-temperature gas resides? The answer to this question can be found in Figure 2a. After the formation of the massive central seed, the gas inflow into the central 2 pc is minimal, while \dot{M} is high into the outer disk (see also Fig. 4). The mass within the region, $R \lesssim 20$ pc, is dominated by the central seed and by the DM that was dragged inward by collapsing gas, in adiabatic contraction. The ratio of the gravitational acceleration due to the gas to that of the central seed, $M_{\text{gas}}(< R)/M_{\text{seed}}$ is $< 10^{-2}$ for the

inner disk and $< 10^{-1}$ for the outer disk, even at the end of the simulation.

The necessary condition for the gas to collapse in the presence of a tidal field is that its density has to exceed the mean density associated with the tidal field. In our case this leads to the Roche limit radius of ~ 10 pc. Moreover, Toomre’s parameter $Q \gg 1$ in both disks, due to the presence of the central seed, and the cooling floor temperature of atomic gas. The penetrating filaments also inject gas and stir turbulent motions in the outer disk (Fig. 9). So, at least for ~ 10 Myr after the formation of the seed, and until the gas builds up anew in the region (Fig. 2b), the fragmentation in the disks will be heavily suppressed.

To visualize the morphology of the gas inflow, we produce density slices in three projection planes, xy , yz and xz , using nested boxes, from 4 kpc on a side to 10 pc, at $t \sim 369$ Myr (Fig. 8). The inner and outer disks are visible in the last two frames, i.e., 40 pc and 10 pc. The inner disk is geometrically-thin and seen edge-on in the xy and yz planes and face-on in the xz plane. It is surrounded by the geometrically-thicker disk, whose mid-plane is inclined to that of the inner disk by about 45° in the yz plane. Spiral structure is clearly observed in both disks. The accreting gas is shocked at the disk surface, as can be seen in the bottom frames of Figure 9 (left and middle columns). Similar behavior has been observed by Choi et al. (2013) for isolated models of direct collapse.

3.3 Evolution of angular momentum in the accretion flow: understanding the dynamical consequences of the massive seed

An alternative way to view the growing disk in the center is to study the evolution of the angular momentum in the collapsing flow (Fig. 10). We show the specific angular momentum profile, $j_{\text{gas}}(r)$, at four representative times. For

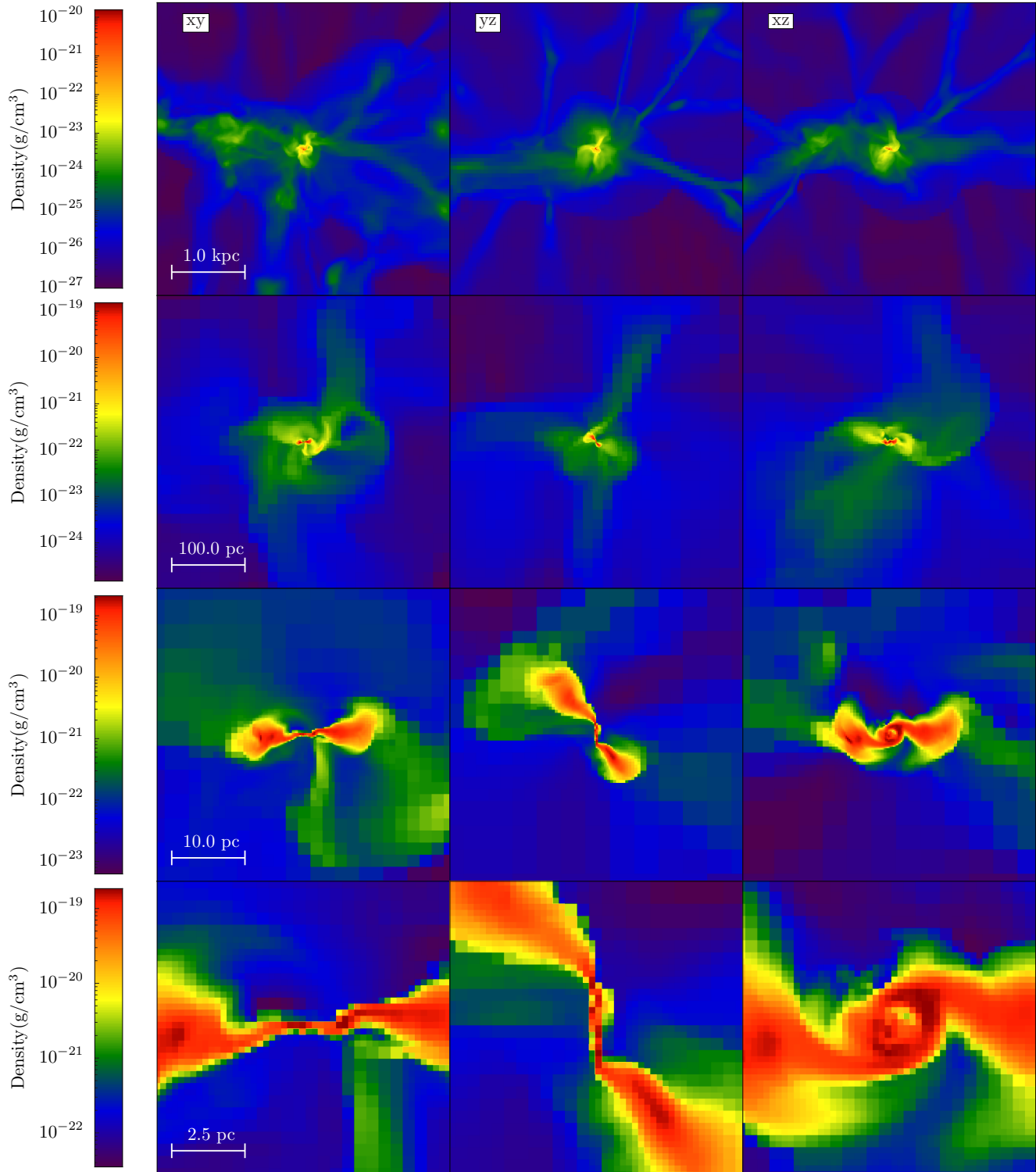


Figure 8. Gas density slices in three projections at the end of the simulation, $t \sim 369$ Myr, for run L12. The frames spanning 40 pc and 10 pc (on a side) exhibit prominent disk features with the xy and yz planes displaying nearly edge-on views, and the xz plane showing a nearly face-on view of the forming disk around the most massive sink particle.

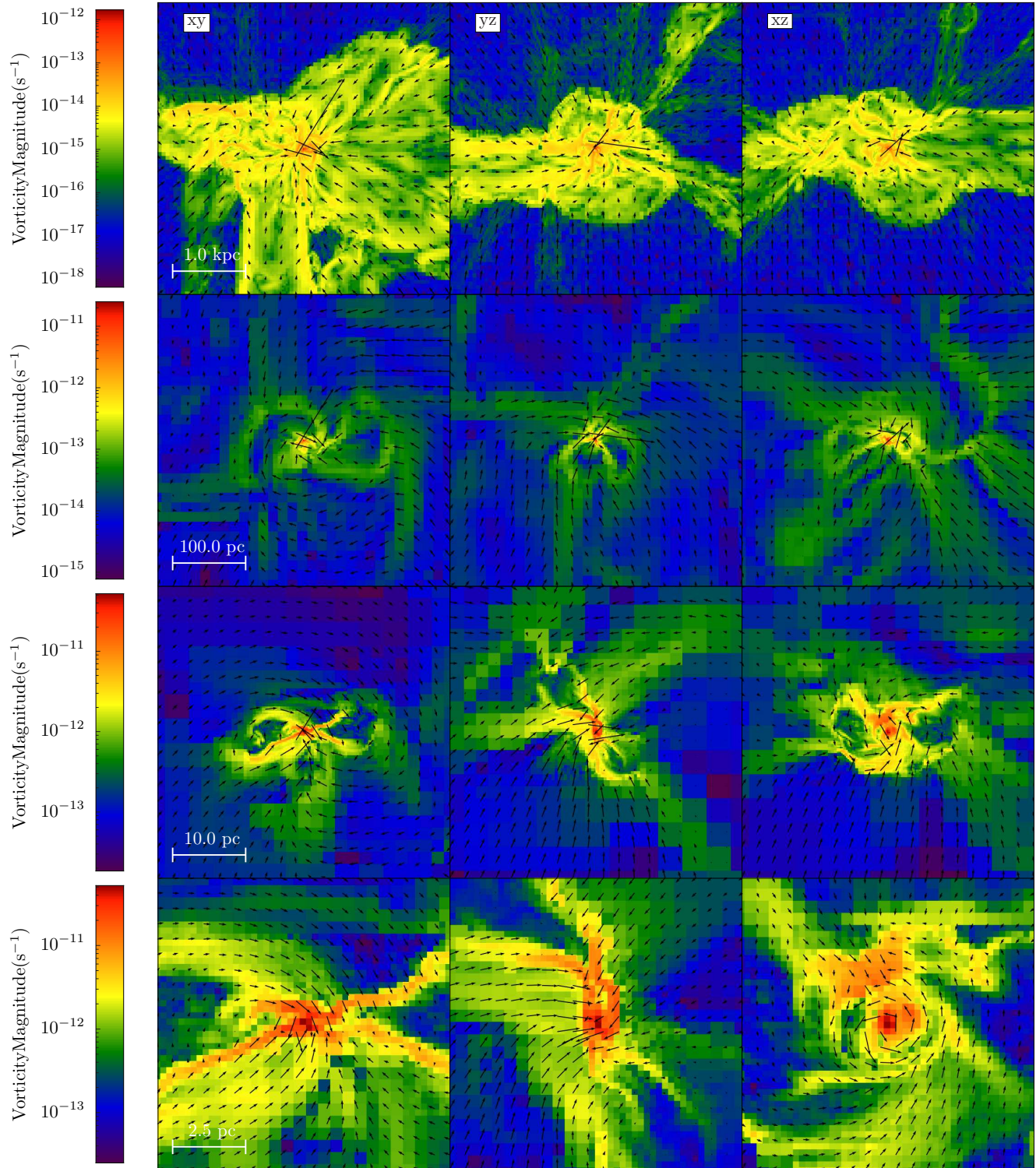


Figure 9. Vorticity magnitude slices of the gas evolution with projected velocity arrows, at the end of the simulation, $t \sim 369$ Myr, for run L12. Velocity arrows confirm the dominant rotation in the xz plane. Arrows in the xy and yz planes show a shock forming at the disk surfaces in the gas which is accreted from outside the disk plane.

comparison, we also plot the circular angular momentum profiles, $j_c(r)$. Initially, the gas has $j_{\text{gas}} \ll j_c$, but increases its specific angular momentum with time, as more gas starts to move inward. For $t = 365.9$ Myr, the gas inside ~ 10 pc radius from the seed exhibits a nearly maximal allowable rotation, $j_{\text{gas}} \sim j_c$ — a clear signature that the disk completely dominates the kinematics in this region.

We now turn to the main mechanism of angular momentum loss by the gas. If angular momentum were conserved during the collapse, the gas within the dominant DM halo potential would be able to collapse only by a factor of ~ 10 before forming a disk (e.g., Shlosman 2013, and refs. therein). However, the shapes of growing DM halos are inherently triaxial, as seen in virtually all numerical simulations (e.g., Allgood et al. 2006; Berentzen et al. 2006). The gravitational torques which result from such halos remove angular momentum from the gas and allow the collapse to proceed (e.g., Berentzen & Shlosman 2006). This happens even in regions where the gas has decoupled from the DM, because for non-axisymmetric mass distributions, the external mass can impose torques on smaller radii.

We have verified the importance of gravitational torques on large and small spatial scales in cosmological simulation of direct collapse (Choi et al. 2015). On larger scales, $r \sim 10 - 50$ pc, we have extended this analysis for another ~ 10 Myr, in the presence of the massive central seed (Fig. 11, left frame). A careful inspection of this region shows that the high amplitude of the $m = 2$ mode has its origin in a pair of dominant filaments, which feed the outer disk at a high mass accretion rate. So, indeed, the development of the $m = 2$ mode with some non-negligible amplitude is expected here. Prior to the formation of the central seed, the gas on these scales responds to the torques from the DM halo, and its response is that of a self-gravitating fluid. However, after $t \sim 362$ Myr, the radius of influence of the seed is about $r_{\text{infl}} \sim 43 M_{\text{seed},6} v_{\text{vir},10}^{-2}$ pc, where $M_{\text{seed},6}$ is the seed mass in units of $10^6 M_{\odot}$, and $v_{\text{vir},10}$ is the DM halo virial velocity in units of 10 km s^{-1} . Hence, almost immediately after its formation, the central seed dominates the dynamics of the region hosting the disks. After this time, the gas response to the external torques, both hydrodynamical and gravitational, is that of a non-self-gravitating fluid.

The morphological evolution of the outer disk is, therefore, dominated by the mass influx along the filaments. Without this perturbation, the disk would become largely axisymmetric, but as the deprojected image of the face-on outer disk shows (Fig. 11, middle frame), it is dominated by spiral modes, from $m = 2$ to higher harmonics, with substantial amplitudes. The inner disk, within a cylindrical annulus $0.5 \lesssim r \lesssim 2$ pc, and thickness $\Delta z = 0.5$ pc, exhibits a lower amplitude $m = 2$ and 1 responses (Fig. 11, right frame), and is affected by the filaments to a smaller extent. Note that the misalignment of the two disks itself can in principle produce gravitational torques and induce $m = 2$ density modes, albeit heavily diluted by the central seed.

Thus, the self-gravity of both disks is severely diluted by the gravity of the massive seed in the center. The outer disk is perturbed by the pair of external filaments which maintains the $m = 2$ symmetry there. The inflow rate that reaches the inner disk is much smaller, comes mostly from the outer disk (with infall along the rotation axis), and appears more axially symmetrized.

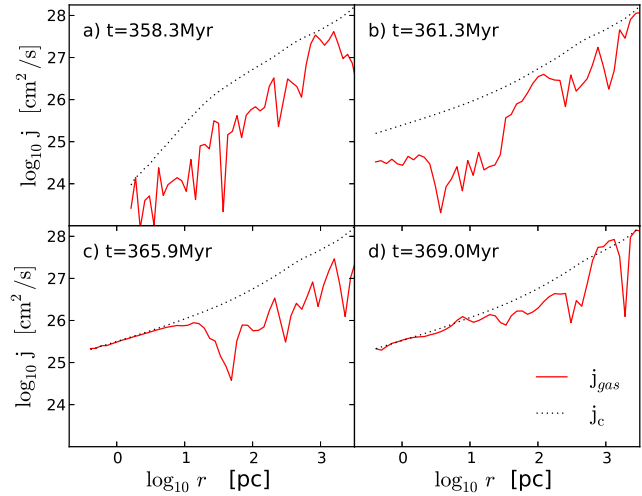


Figure 10. Evolution of the specific angular momentum profile in the gas, $j(r)$, for run L12 at 358.3 Myr (top left), 361.33 Myr (top right), 365.9 Myr (bottom left), and 369.0 Myr (bottom right). The angular momentum is measured in a cylindrical volume with a thickness of 10 pc, with respect to the rotation axis of the inner disk, which happens to nearly coincide with the y -axis of the computational box. The dotted lines represent the instantaneous Keplerian specific angular momentum profiles. Note that the innermost j_{gas} reaches its Keplerian value at later times.

How stable is the configuration of misaligned disks and why did it form in the first place? The answer to the latter question is that the misaligned disks form in response to the variable angular momentum axis in the accretion flow. Future simulations will show whether this configuration is limited to a pair of disks, or whether additional misaligned rotating flows can form at larger radii. The reason for its apparent stability is found in the two filaments which feed the outer disk. By the end of the simulation, $t \sim 369.12$ Myr, these filaments have been substantially degraded, and so one can expect that the disks will re-align themselves. But gravitational torques between the disks are severely diluted by the central seed, which helps to prolong the life of this configuration. Of course, continuing collapse will add additional mass to the region, and one cannot predict a priori what will be the direction of its angular momentum vector.

To summarize, the massive seed fundamentally transforms the character of the accretion flow, to a large extent independently of the numerical resolution, once the radius of influence of this seed is resolved. Most importantly, as long as it dominates gravitationally, the massive seed dilutes the self-gravity of the gas, damps fragmentation, decreases substantially the angular momentum transfer away from the gas, and, therefore, leads to the formation of a disk(s) in its vicinity. The scale chosen to break the self-similar collapse in our runs, given by the condition to create sink particles, determines the position of the disk flow at $\sim 0.01 - 10$ pc. Increasing or decreasing this scale would move the disk inward or outward, respectively, but the appearance of such a flow is generic.

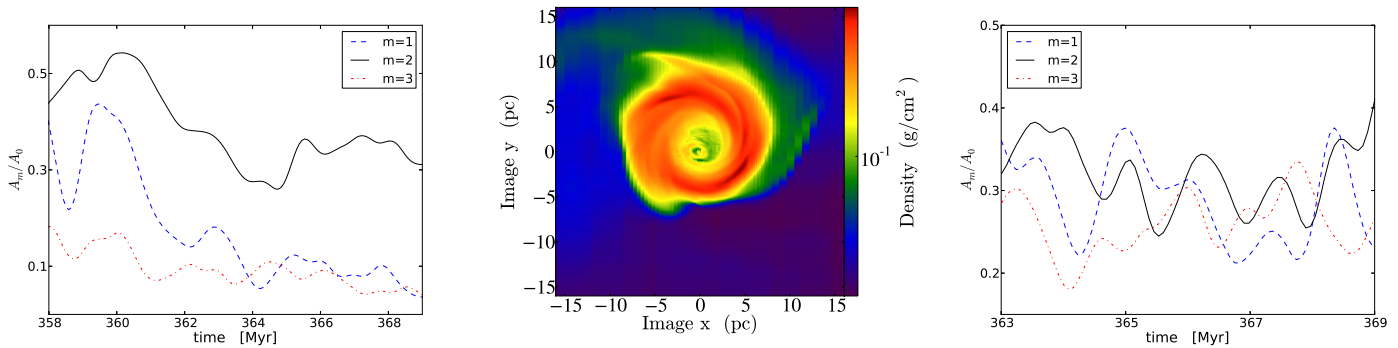


Figure 11. Evolution of the nonaxisymmetric modes on progressively smaller spatial scales — in the region dominated by the filaments, and in the outer and inner disks. *Left:* Evolution of the Fourier gas density modes $m = 1, 2,$ and 3 , normalized to the $m = 0$ mode amplitude for run L12 in the penetrating filaments region. The amplitudes are measured within the cylindrical annulus defined by $r \sim 10 - 50$ pc and thickness $\Delta z = 10$ pc. *Middle:* Face-on outer disk and inclined inner disk at the end of the simulation, $t = 369.12$ Myr. Note the effect of the outer filaments penetrating the disk and driving $m = 2$ and higher modes in the form of spirals. *Right:* Evolution of the Fourier gas density modes $m = 1, 2,$ and 3 , normalized to the $m = 0$ mode amplitude for run L12 in the face-on inner disk. The amplitudes are measured within the cylindrical annulus defined by $r \sim 0.5 - 2$ pc and thickness $\Delta z = 0.5$ pc.

3.4 Evolution of turbulent motions in the accretion flow

It is more difficult to recognize the two-disk system in the vorticity magnitude slices displayed in Figure 9. Nevertheless, the face-on and edge-on inner disk appears prominent in the yz and xz projection planes in the bottom frames. For the edge-on projections of this disk one observes accretion flows that are directed along its rotation axis. These flows appear to be highly turbulent. Generally, the vorticity increases toward the center, as the vorticity maps show on various spatial scales. The flow is turbulent both away from the outer disk and in its vicinity, though closer to the outer disk mid-plane the turbulence decays. Further analysis of the developing turbulence in the collapsing flow will be presented elsewhere.

4 DISCUSSION

We have used cosmological zoom-in simulations with the AMR Enzo code to study the long-term evolution of direct collapse that can lead to the formation of SMBH seeds at high redshifts. To circumvent the Courant condition on the timestep we have invoked the sink particle method. Sink particles are introduced when the refinement criterion has been violated and the resolution becomes insufficient at the highest refinement level (see Section 2). The innermost accretion flow on scales of $\lesssim 1$ pc forms a number of sink particles after ~ 361.5 Myr. They have been permitted to grow by accretion and merging. By comparing various spatial resolutions, we find that allowing for a maximum of 12 refinements, corresponding to 0.1 pc resolution, is sufficient to obtain the convergence in the growth rate of the central sink particle, i.e., this growth rate remains unchanged when the resolution is increased. Under these conditions, we have been able to prolong the evolution of the collapsing gas by another 10 Myr, compared to Choi et al. (2015), who stopped the simulations at $t = 360.13$ Myr ($z \sim 12$) after the Big Bang. Our main results show that,

- The masses of these sink particles have remained below $\sim 10^3 M_\odot$, with the exception of the central particle which grows rapidly to $M_{\text{seed}} \sim 2 \times 10^6 M_\odot$ in less than ~ 2 Myr, due to gas accretion and merging with other particles.
- This growth coincides with the cessation of gravitational collapse on sub-pc scales and the formation of two misaligned gas disks — the inner one after ~ 361.5 Myr, and the outer one after ~ 363.7 Myr.
- Formation of misaligned disks is related to the variability of the angular momentum direction in the region.
- As we discuss below (see also Section 3.2), the appearance of the massive object (hereafter central seed) in the center is responsible for the cutoff of collapse.
- On larger scales, however, the collapse continues unimpeded. At this point, we make no assumptions about the nature of this massive object, but note that its rapid formation confirms the feasibility of this path to an SMBH.

We have analyzed the co-evolution of the flow with the growth of the central seed, on scales comparable to the size of the forming disk. For this purpose, we have computed the evolution of Fourier modes on scales $\sim 0.5 - 2$ pc in the inner disk, $2.5 - 10$ pc in the outer disk, and $10 - 50$ pc outside the disk system. The low $m = 1$ to 3 mode amplitudes remain moderate, in the range of $0.2 - 0.4$ (relative to $m = 0$) in the inner disk, and the outer disk is dominated by $m = 2$ spiral modes. They do not show any additional growth which can be expected if the fluid is self-gravitating. In both disks, we estimate that gas self-gravity is not important in comparison with the gravitational acceleration due to the massive central seed, and show that the fragmentation in the disks is damped due to the sharp increase of the Jeans masses there, after the formation of the massive seed (Section 3.2). In other words, the disks lie within the Roche limit of the central seed. However, the inflow into the outer disk is dominated by a pair of filaments which maintain the $m = 2$ perturbation for a long time, while shear tends to axisymmetrize it. The mass inflow there is high, $\dot{M} \sim 0.3 M_\odot \text{yr}^{-1}$. The inner disk is fed at a much smaller rate, $\dot{M} \lesssim 10^{-2} M_\odot \text{yr}^{-1}$, by the outer disk. Under these conditions of severely diluted

self-gravity, mode-coupling does not operate and the non-axisymmetric (and mostly $m = 2$) modes quickly saturate (e.g., Christodoulou et al. 1995).

Because the innermost accretion rate is substantially below that on larger spatial scales, the gas will accumulate in the disks, as discussed in section 3.2 and shown in Figure 2. We expect that this mass growth can lead to some local gravitational instabilities in the disks, but not to the resumption of a massive accretion onto the central seed.

A number of important issues are related to this evolution. Probably the most interesting one is how the collapse proceeds on smaller scales — this has been deliberately ignored in the current work, with the introduction of the seed particle algorithm. We anticipate that the cessation of the accretion process observed here justifies our conclusion that the characteristic mass of the forming SMBH seed is $M_{\bullet} \sim 10^6 M_{\odot}$.

Another issue is related to the fate of the inclined disks configuration, which formed as a result of gas flowing into the region with a variable orientation of angular momentum. Most probably this configuration will be destroyed by the same process that created it in the first place. In any case, if the SMBH seed forms before the next spike in the accretion rate, the radiation and/or mechanical feedback could already modify substantially the conditions in the inflowing gas.

The presence of the massive central object, can be favorable for the growth of the $m = 1$ mode in the surrounding accretion disk, when the disk mass is *not* negligible compared to the massive object — hence when disk self-gravity is not severely diluted by the object (e.g., Adams et al. 1989). Furthermore, for *stellar* disks, which are dominated by the central object and hence reside in the Keplerian potential, the $m = 1$ mode, when triggered, can be long-lived, due to the absence of precession in this potential (Tremaine 1995). Under these conditions, the individual stellar orbits can be weakly “glued” by their gravitational attraction and can maintain this non-axisymmetric mode. This mode has been suggested to be responsible for the mass accretion rate onto the SMBH under certain conditions (Hopkins & Quataert 2010).

However, one expects that the $m = 1$ mode will not be able to grow when strong time-dependent perturbations are present, which destroy the orbital correlations in the Keplerian gaseous disk, i.e., in a disk with the ratio of the central mass-to-disk mass much greater than unity. We do not observe any substantial growth of $m = 1$ mode and any mass accretion flux associated with this mode.

Fast growth of the central object will have dynamical consequences for the collapsing flow. Among these, the most important appears to be the *inability* of the flow to get rid of its angular momentum. Gravitational torques from the DM serve as the main mechanism extracting angular momentum from the gas, but close to the massive central seed, the torques are diluted by the gravitational monopole and become inefficient. The gas acquires rotational support and settles in a disk-like configuration around the center. Its fragmentation is damped by the tidal forces of the central seed in the presence of the floor temperature of atomic gas.

Damping of the nonaxisymmetric instabilities in the disk leads to the inability of the gas to transfer its angular momentum to the outer gas or to the surrounding DM.

This results in the accumulation of gas in this region and the growth of the disk. In fact, the rapid growth of the central object is the prime cause of the formation of the disks on these scales and of their lack of fragmentation. After the initial period of rapid growth, the massive central object continues to grow but at a much slower pace, by a factor of $\sim 2 - 3$ (Fig. 1).

The corollary of this evolution is the formation of a massive object in the center of the direct collapse region. The resolution scale in our model is chosen somewhat arbitrarily, just to allow for the second stage of the collapse to be resolved spatially. But our results bring up an important issue: how does the nature of the accretion flow changes with the formation and growth of the central massive object? The resulting formation of the gaseous disk around this object is a direct consequence of dramatically reduced efficiency of angular momentum transfer within the radius of influence of the massive center, R_{infl} (Section 3.3). Of course the compactness parameter of such an object, $M_{\text{seed}}/R_{\text{seed}}$, where R_{seed} is the seed size, will determine the inner edge of the forming disk, but not the position of its outer edge, as long as it is resolved numerically. Here R_{seed} is the size of the seed or the associated numerical resolution.

We have also assumed that the molecular gas, H_2 , is not present during direct collapse, and, therefore, the floor temperature of the atomic gas lies around a several thousand degrees. We justify this by the presence of the Lyman-Werner continuum which originates in nearby stellar populations (e.g., Agarwal & Khochfar 2015) or in situ (Choi et al. 2013).

Another important issue is our neglect of the radiation feedback in the region of the disk. To address this, it is crucial to know the nature of the massive object, and the source of the radiation field. If this object is an SMS fueled by the thermonuclear reactions in the core and accretion energy in the envelope (e.g., Begelman 2010), this will specify the effective temperature, spectral energy distribution and geometry of the radiation field. Alternatively, if the SMS stage is bypassed (see Section 1), the rate of locally produced energy will be very different and the radiation field could become anisotropic, with most of it escaping in the preferred direction, i.e., the rotation axis. We also note that very large accretion rates encountered during direct collapse can make the radiation feedback much less efficient dynamically.

ACKNOWLEDGMENTS

We thank Takashi Hosokawa for interesting and insightful discussions, and thank the Enzo and YT support team. All analysis has been conducted using YT (Turk et al. 2011, <http://yt-project.org/>). I.S. acknowledges support from NSF grant AST-0807760 and from HST/STScI grant AR-12639.01-A. I.S. and K.N. are grateful for support from International Joint Research Promotion Program at Osaka University. J.H.C acknowledges support from NASA ATP NNX11AE09G, NSF AST-1009799, and Caltech/JPL SURP Project No. 1515294 through the UT Austin (P.I. Paul Shapiro). M.C.B. acknowledges support from the NSF under AST-1411879. K.N. acknowledges the partial support by JSPS KAKENHI Grant Number 26247022. Support for HST/STScI AR-12639.01-A was provided by NASA through

a grant from the STScI, which is operated by the AURA, Inc., under NASA contract NAS5-26555.

REFERENCES

Abel T., Anninos P., Zhang Y., Norman M. L., 1997, *New Astronomy*, 2, 181
 Abel T., Bryan G. L., Norman M. L., 2002, *Science*, 295, 93
 Adams F. C., Ruden S. P., Shu F. H., 1989, *ApJ*, 347, 959
 Agarwal B., Khochfar S., 2015, *MNRAS*, 446, 160
 Allgood B., Flores R. A., Primack J. R., Kravtsov A. V., Wechsler R. H., Faltenbacher A., Bullock J. S., 2006, *MNRAS*, 367, 1781
 Anninos P., Zhang Y., Abel T., Norman M. L., 1997, *New Astronomy*, 2, 209
 Bate M. R., Bonnell I. A., Price N. M., 1995, *MNRAS*, 277, 362
 Becerra F., Greif T. H., Springel V., Hernquist L. E., 2015, *MNRAS*, 446, 2380
 Begelman M. C., 2010, *MNRAS*, 402, 673
 Begelman M. C., Shlosman I., 2009, *ApJL*, 702, L5
 Begelman M. C., Volonteri M., Rees M. J., 2006, *MNRAS*, 370, 289
 Berentzen I., Shlosman I., 2006, *ApJ*, 648, 807
 Berentzen I., Shlosman I., Jogee S., 2006, *ApJ*, 637, 582
 Berger M. J., Colella P., 1989, *Journal of Computational Physics*, 82, 64
 Bromm V., Larson R. B., 2004, *ARA&A*, 42, 79
 Bromm V., Loeb A., 2003, *ApJ*, 596, 34
 Bryan G. L., Norman M. L., 1997, in *Astronomical Society of the Pacific Conference Series*, Vol. 123, *Computational Astrophysics; 12th Kingston Meeting on Theoretical Astrophysics*, Clarke D. A., West M. J., eds., p. 363
 Bryan G. L., Norman M. L., O’Shea B. W., Abel T., Wise J. H., Turk M. J., Reynolds D. R., Collins D. C., Wang P., Skillman S. W., Smith B., Harkness R. P., Bordner J., Kim J.-h., Kuhlen M., Xu H., Goldbaum N., Hummels C., Kritsuk A. G., Tasker E., Skory S., Simpson C. M., Hahn O., Oishi J. S., So G. C., Zhao F., Cen R., Li Y., Enzo Collaboration, 2014, *ApJS*, 211, 19
 Bryan G. L., Norman M. L., Stone J. M., Cen R., Ostriker J. P., 1995, *Computer Physics Communications*, 89, 149
 Choi J.-H., Shlosman I., Begelman M. C., 2013, *ApJ*, 774, 149
 —, 2015, *MNRAS*, 450, 4411
 Christodoulou D. M., Shlosman I., Tohline J. E., 1995, *ApJ*, 443, 551
 Eisenstein D. J., Hut P., 1998, *ApJ*, 498, 137
 Fan X., Strauss M. A., Schneider D. P., Becker R. H., White R. L., Haiman Z., Gregg M., Pentericci L., Grebel E. K., Narayanan V. K., Loh Y.-S., Richards G. T., Gunn J. E., Lupton R. H., Knapp G. R., Ivezić Ž., Brandt W. N., Collinge M., Hao L., Harbeck D., Prada F., Schaye J., Strateva I., Zakamska N., Anderson S., Brinkmann J., Bahcall N. A., Lamb D. Q., Okamura S., Szalay A., York D. G., 2003, *AJ*, 125, 1649
 Federrath C., Banerjee R., Clark P. C., Klessen R. S., 2010, *ApJ*, 713, 269
 Federrath C., Sur S., Schleicher D. R. G., Banerjee R., Klessen R. S., 2011, *ApJ*, 731, 62
 Gong H., Ostriker E. C., 2013, *ApJS*, 204, 8
 Haehnelt M. G., Rees M. J., 1993, *MNRAS*, 263, 168
 Hahn O., Abel T., 2011, *MNRAS*, 415, 2101
 Haiman Z., Loeb A., 2001, *ApJ*, 552, 459
 Hopkins P. F., Quataert E., 2010, *MNRAS*, 407, 1529
 Hosokawa T., Omukai K., Yoshida N., Yorke H. W., 2011, *Science*, 334, 1250
 Inayoshi K., Omukai K., Tasker E., 2014, *MNRAS*, 445, L109
 Johnson J. L., Khochfar S., Greif T. H., Durier F., 2011, *MNRAS*, 410, 919
 Krumholz M. R., McKee C. F., Klein R. I., 2004, *ApJ*, 611, 399
 Latif M. A., Schleicher D. R. G., Schmidt W., Niemeyer J., 2013, *MNRAS*, 433, 1607
 Latif M. A., Zaroubi S., Spaans M., 2011, *MNRAS*, 411, 1659
 Li Y., Hernquist L., Robertson B., Cox T. J., Hopkins P. F., Springel V., Gao L., Di Matteo T., Zentner A. R., Jenkins A., Yoshida N., 2007, *ApJ*, 665, 187
 Mayer L., Kazantzidis S., Escala A., Callegari S., 2010, *Nature*, 466, 1082
 Milosavljević M., Bromm V., Couch S. M., Oh S. P., 2009, *ApJ*, 698, 766
 Mortlock D. J., Warren S. J., Venemans B. P., Patel M., Hewett P. C., McMahon R. G., Simpson C., Theuns T., González-Solares E. A., Adamson A., Dye S., Hambly N. C., Hirst P., Irwin M. J., Kuiper E., Lawrence A., Röttgering H. J. A., 2011, *Nature*, 474, 616
 Navarro J. F., Frenk C. S., White S. D. M., 1997, *ApJ*, 490, 493
 Norman M. L., Bryan G. L., 1999, in *Astrophysics and Space Science Library*, Vol. 240, *Numerical Astrophysics*, Miyama S. M., Tomisaka K., Hanawa T., eds., p. 19
 Oh S. P., Haiman Z., 2002, *ApJ*, 569, 558
 Omukai K., 2001, *ApJ*, 546, 635
 Pelupessy F. I., Di Matteo T., Ciardi B., 2007, *ApJ*, 665, 107
 Planck Collaboration, Ade P. A. R., Aghanim N., Arnaud M., Ashdown M., Aumont J., Baccigalupi C., Banday A. J., Barreiro R. B., Bartlett J. G., et al., 2015, *ArXiv:1502.01589*
 Prieto J., Jimenez R., Haiman Z., 2013, *MNRAS*, 436, 2301
 Schleicher D. R. G., Spaans M., Glover S. C. O., 2010, *ApJL*, 712, L69
 Shlosman I., 2013, in *Secular Evolution of Galaxies*, Falcón-Barroso J., Knapen J. H., eds., pp. CUP, 555
 Spaans M., Silk J., 2006, *ApJ*, 652, 902
 Sugimura K., Omukai K., Inoue A. K., 2014, *MNRAS*, 445, 544
 Sur S., Schleicher D. R. G., Banerjee R., Federrath C., Klessen R. S., 2010, *ApJL*, 721, L134
 Teyssier R., Moore B., Martizzi D., Dubois Y., Mayer L., 2011, *MNRAS*, 414, 195
 Tremaine S., 1995, *AJ*, 110, 628
 Truelove J. K., Klein R. I., McKee C. F., Holliman II J. H., Howell L. H., Greenough J. A., 1997, *ApJL*, 489, L179
 Turk M. J., Oishi J. S., Abel T., Bryan G. L., 2012, *ApJ*, 745, 154
 Turk M. J., Smith B. D., Oishi J. S., Skory S., Skillman S. W., Abel T., Norman M. L., 2011, *ApJS*, 192, 9
 Volonteri M., Rees M. J., 2006, *ApJ*, 650, 669

- Wang P., Li Z.-Y., Abel T., Nakamura F., 2010, ApJ, 709,
27
Wise J. H., Turk M. J., Abel T., 2008, ApJ, 682, 745
Wu X.-B., Wang F., Fan X., Yi W., Zuo W., Bian F., Jiang
L., McGreer I. D., Wang R., Yang J., Yang Q., Thompson
D., Beletsky Y., 2015, Nature, 518, 512